State of health prediction of lithium-ion batteries based on SSA optimized hybrid neural network model.

ZHOU, J., WANG, S., CAO, W., XIE, Y. and FERNANDEZ, C.

2024

State of Health Prediction of Lithium-ion Batteries Based on SSA Optimized Hybrid Neural Network Model

Jiani Zhou[a], Shunli Wang[a,b*], Wen Cao[a], Yanxin Xie[a], Carlos Fernandez[c]

([a] School of Information Engineering, Southwest University of Science and Technology, Mianyang 621010, China;

[b] School of Electrical Engineering, Sichuan University, Chengdu 610065, China;

[c] School of Pharmacy and Life Sciences, Robert Gordon University, Aberdeen AB10-7GJ, UK)

Abstract: The accurate state of health (SOH) estimation of lithium-ion batteries (LIBs) is crucial for the operation and maintenance of new energy electric vehicles. To address this current problem, an improved hybrid neural network model for SOH prediction based on a sparrow search algorithm (SSA) optimized convolutional bi-directional long short-term memory neural network (CNN-Bi-LSTM) is proposed. Firstly, by analyzing the battery aging data, several feature indicators with highly correlated battery life degradation are constructed. Secondly, the CNN-Bi-LSTM model is used to extract the battery aging data features and the latent timing laws. Finally, the SSA optimizes the parameters to improve the model accuracy. Experimental results based on the NASA-Pcoe battery dataset show that the SSA-CNN-Bi-LSTM model outperforms other models, and the root-mean-square errors of the SOH prediction results are all less than 0.6%. It indicates that the proposed SSA-CNN-Bi-LSTM model is capable of predicting SOH accurately and with high precision.

Keywords: Lithium-ion batteries; State of health; Convolutional neural network; Bi-directional long short-term memory; Sparrow search algorithm.

Corresponding author: Shunli Wang. Tel/fax: +86-15884655563. E-mail address: 497420789@qq.com.

1. Introduction

In recent years, the massive consumption of traditional fossil energy has led to serious air pollution and the greenhouse effect, and the problem of energy shortage is becoming more and more serious [1, 2]. To effectively alleviate environmental pollution and solve the energy crisis, energy development is gradually transformed in the green direction [3-5]. New energy electric vehicles with zero road emissions and low energy consumption have gradually come into

people's view and have become an important direction for the development of the automobile industry today.

Compared with other energy storage devices, LIBs are widely used for its high safety, low self-discharge rate, no memory effect, long cycle life, low pollution, high energy density, good stability, and many other advantages [5, 6]. LIBs are gradually becoming the main source of energy supply for the new generation of new energy vehicles [7, 8]. During the use of batteries, complex chemical reactions occur within the battery, leading to aging of the diaphragm, and depletion of the electrode material and electrolyte solution [9, 10]. Figure 1 shows the principle of the aging mechanism of LIBs. With time accumulation, the stability and safety of the battery will be reduced, thus leading to the occurrence of safety accidents, and greatly restricting the development of LIBs [11-14]. The SOH of LIBs changes during the actual charging and discharging cycles of the battery, and its capacity decreases leading to a gradual degradation of performance [15, 16]. If the battery reaches the capacity failure threshold and safety measures such as replacement or maintenance are not taken in time, it may cause serious safety accidents [17, 18]. Therefore, the research on capacity degradation and SOH prediction during the use of LIBs is becoming a hot spot in the field of battery measurement and control research at home and abroad.

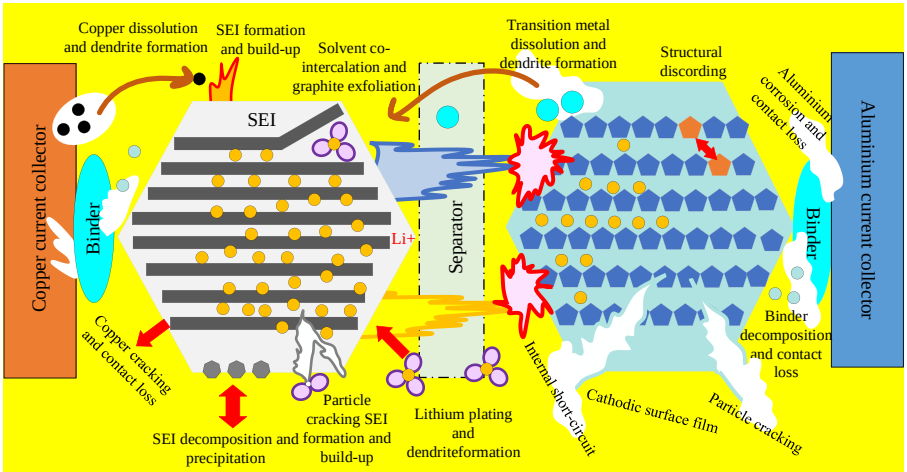

Figure 1. Aging mechanism of lithium-ion batteries

Indicators affecting the aging of LIBs can be categorized into external and internal indicators, such as the electrochemical properties of the battery, the manufacturing process, and operating environmental conditions [19-21]. The most visual manifestation of the battery aging process is the decline of available energy and power performance, and reflected in the internal

battery is the decrease of battery capacity and the increase of internal resistance [22-24]. The SOH prediction is usually to analyze and summarize the data of LIBs usage conditions and historical health status and use relevant algorithms to explore the intrinsic law of battery life decline, to predict the future decline trajectory of the battery [25-28]. Currently, the prediction methods for SOH of LIBs are mainly divided into based on mechanism model methods and based on data-driven methods.

The prediction method based on the mechanism model is to simulate the electrochemical mechanism between the materials inside the battery, thus indirectly simulating the battery charging, discharging, and aging behaviors to give the form of performance degradation [29-31]. Then, the SOH estimates are predicted by determining the optimal parameters of the model based on the changes in the properties of the electrode materials. T.R. Ashwin et al. [32] developed a pseudo-two-dimensional (P2D) electrochemical lithium-ion battery model based on electrochemical theory. The growth of the solid electrolyte interface (SEI) layer is estimated at different cutoff voltages and charging current rates, and the main reason for the capacity degradation of the battery is the generation of SEI film at the electrolyte boundary, and the prediction of SOH of the battery is realized. Allam et al. [33] developed an empirical model for internal resistance growth based on electrochemical impedance spectroscopy test data combined with SOH prediction of batteries using the Particle Filter (PF) algorithm. The data-driven approach is directly extracted from the decline history data of LIBs that can characterize the battery degradation health indicators, and combined with intelligent algorithms to deeply explore the battery's life decay behavior, and realize the SOH of LIBs [34-39]. Long et al. [40] implemented SOH prediction of LIBs using an AR model optimized by particle swarm optimization (PSO) algorithm. Qin et al. [41] used a deep belief network (DBN) to train the historical capacity data of the battery and the discharge capacity data of the battery in each cycle to capture the decreasing trend of the discharge capacity of the battery and predict the SOH of the battery.

The degradation information of LIBs belongs to time series, and the Long Short Term Memory (LSTM) neural network, as one based on data-driven, can effectively improve the temporal analysis of lithium battery data [19, 42-44]. Tuo Ji et al. [45] developed an LSTM model of battery capacity to realize SOH estimation over the whole life cycle of LIBs at

different temperatures and under different operating conditions. To achieve parallel processing of time series data and to improve the model computational accuracy and running speed [46, 47]. Yu Guo et al. [48] proposed an SOH estimation method based on the Bi-LSTM model. This method solves the problem of unidirectional data transfer of LSTM and realizes the bidirectional propagation of past information and future information, but the feature extraction ability of input data is weak [49-51]. Due to the strong ability of CNN to extract high-dimensional features of the input data [52, 53], Shuo Sun et al. [54] proposed a CNN-Bi-LSTM fused SOH prediction model, and selected the isobaric discharge time as the health factor to train the battery capacity degradation model. However, the structural parameters of the model are subjectively set by humans, leading to poor model prediction accuracy [55-59]. Li Cao et al. [60] compared SSA with other swarm intelligence algorithms and found that the optimal and average solutions of SSA are higher than other swarm intelligence algorithms and the late convergence speed is accelerated. Thus, SSA has more high-performance global parameter search capability than other algorithms.

Combining the shortcomings in the above studies, this paper proposes a high-precision prediction method for the SOH of LIBs using the SSA to optimize the CNN-Bi-LSTM hybrid neural network model. The main contributions of this article are as follows:

(1) To explore the relationship between capacity and battery SOH through the NASA-Pcoe battery dataset, several feature indicators strongly correlated with battery aging are extracted from LIBs charge/discharge curves. Pearson correlation analysis is used to quantify the degree of association between the characteristic indicators and capacity decline, and the features with high correlation are retained, which helps to improve the SOH estimation accuracy.

(2) Aiming at the current problem of low accuracy of SOH prediction for LIBs, a hybrid neural network model combining CNN and Bi-LSTM is constructed for SOH prediction of LIBs. The model utilizes CNN to quickly extract sequence relationships between battery data, and Bi-LSTM can simultaneously capture spatial feature relationships between data dimensions, thus increasing the generalization ability of the model.

(3) To solve the issue of low accuracy of model structure parameters due to human subjective settings, SSA is used to optimize the initial parameters of the model network

structure to achieve a high-precision estimation of SOH for LIBs and effectively extend the battery service life.

(4) The SSA-CNN-Bi-LSTM model inputs the extracted feature indicators and the actual battery capacity, and the trained model performs SOH prediction. The capacity data output from the model prediction is subjected to SOH analysis, and the accuracy and robustness of the model are verified by comparing it with other single models.

In the rest of this article, the experimental battery dataset and feature indicators analysis are described in Section 2. The basic principles and structure of the proposed SSA-CNN-Bi-LSTM model for SOH prediction of LIBs are presented in Section 3. The method is experimentally validated and analyzed for SOH prediction effectiveness and accuracy in Section 4. Finally, this study is summarized and prospected in Section 5.

2 Experimental data and multi-feature indicators analysis

In this section, the data of LIBs charging and discharging process are analyzed and multi-feature indicators are extracted. Then, the degree of correlation between the extracted feature indicators and the battery capacity is analyzed and evaluated using Pearson correlation analysis to further verify the validity of the proposed feature indicators.

2.1 Experimental data description

The study uses the NASA battery public dataset published by the NASA Ames Centre of Excellence for Prediction database. Select one of the datasets containing four 2Ah rated 18650 LIBs and the batteries are numbered B5, B6, B7, and B18. This group of batteries in the external environment and the measurement method is the same, each of the work environments of the battery and charging and discharging stage of the voltage and current operating data as shown in Table 1.

Table 1. Operating conditions for the aging process of LIBs

Battery	Temperature (□)	Charging process		Discharging process	
		Current (A)	Cutoff voltage（V）	Current（A）	Cutoff voltage（V）
B5	24	1.5	4.2	2	2.7
B6	24	1.5	4.2	2	2.5
B7	24	1.5	4.2	2	2.2
B18	24	1.5	4.2	2	2.5

Under the environment temperature of 24□ for the battery cycle aging test, the battery charging process is firstly charged with constant current (CC) for a while, and then charged with constant voltage (CV). The specific charging method is as follows: first charge with a CC of 1.5A until the voltage reaches the charging cut-off voltage of 4.2V; then charge with a CV of 4.2V until the current drops to the cut-off current of 20mA. During the battery discharge process, the battery is discharged in CC mode at a current of 2A until the battery voltage drops to the corresponding cut-off voltage. During each charge/discharge process, parameters such as temperature, voltage, and current are monitored and recorded. SOH is usually defined as a percentage reflecting capacity degradation, characterizing the degree of decline of LIBs, as shown in Equation (1).

$$SOH = \frac{C_{aged}}{C_{rated}} \times 100\% \tag{1}$$

In Equation (1), C_{aged} and C_{rated} denote the current actual available capacity and the factory-rated capacity of the LIBs, respectively. If the actual available capacity of the current battery accounts for a larger share, the higher the SOH prediction value of the LIBs, indicating that the current battery is in a better SOH.

With the increasing number of battery charge/discharge cycles, the active material inside the battery will be gradually lost, which leads to the continuous decay of the battery cycle life and capacity. The complete capacity decay curves of the four numbered LIBs selected for the experiment are shown in Figure 2.

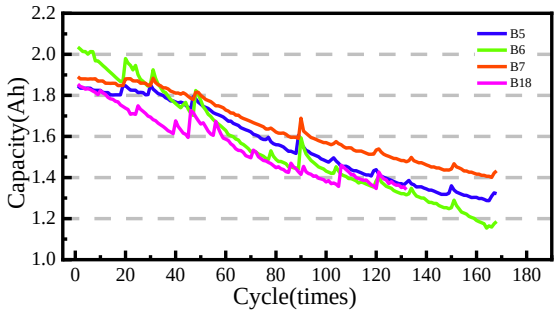

Figure 2. Capacity degradation curves of different batteries

From the graph in Figure 2, it can be seen that with the increase in the number of cycles, the decay process of the capacity of LIBs is nonlinear, showing the phenomenon of global decline and partial regeneration changes. The transient regeneration phenomenon in the capacity decay process will affect the estimation of the capacity value, indicating that the

battery aging process is very complicated. LIBs numbered B5, B6, B7, and B18 reflect different initial capacities and health states. The battery cycle life ends when the decay drops below 80% of the rated capacity.

2.2 Multi-feature indicators extraction

Due to the complexity of the chemical reaction process inside the lithium-ion battery, it is not possible to carry out intuitive and clear measurement descriptions and calculations. Thus, it is necessary to pre-process the raw experimental data to extract the health feature indicators that can characterize the aging of LIBs.The FI extraction flowchart is shown in Figure 3.

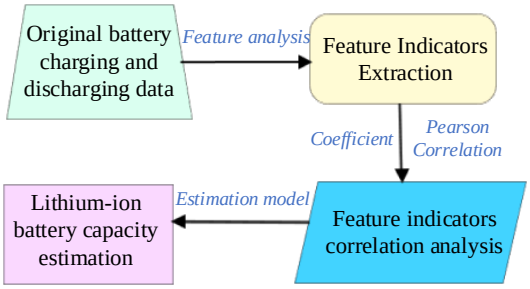

Figure 3. The flowchart of FI extraction

By analyzing the original LIBs charge/discharge data, relevant voltage, current, and other data are extracted. The relevant feature parameters are screened out as feature indicators. Then, the relationship between FI and actual capacity recession is established and the correlation analysis is performed, followed by verifying the degree of correlation. Finally, the new FI is used to estimate the battery capacity, and compared with the actual capacity for analysis. Taking the B5 battery group as an example, the voltage and current curves of the battery during charging and discharging are shown in Figure 4(a) and (b).

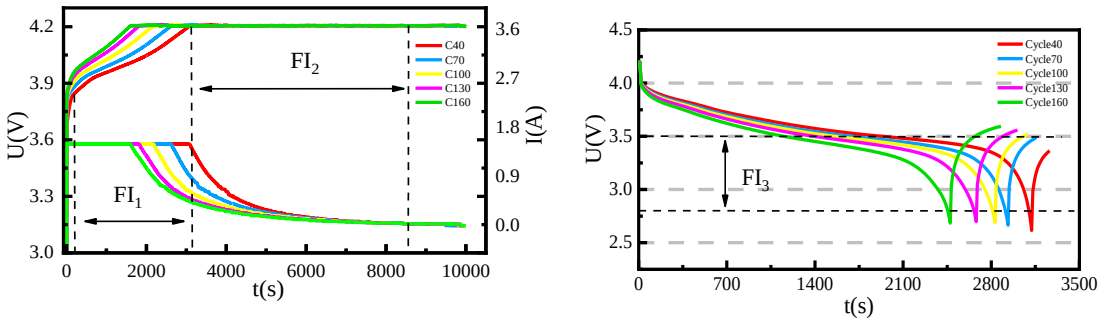

(a) (b)

Figure 4. Charge and discharge stages of the B5 battery with voltage and current change curves.

(a) Charge current and voltage; (b) discharge voltage.

With the increase in the number of cyclic charging and discharging, the active material inside the battery is continuously consumed, and this leads to regular changes in the voltage

and current curves during the charging and discharging of the battery. Thus, in this study, the feature indicators of the internal and external health of the battery will be selected from the charging and discharging curves.

FI_1: Constant current charging time (CCCT)

Figure 5 shows the comparison of battery capacity and CCCT trend with the number of cycles, the CCCT of LIBs after 160 cycles is significantly lower than the CCCT after 40 cycles, and the battery capacity corresponding to the number of cycles is also decreasing.

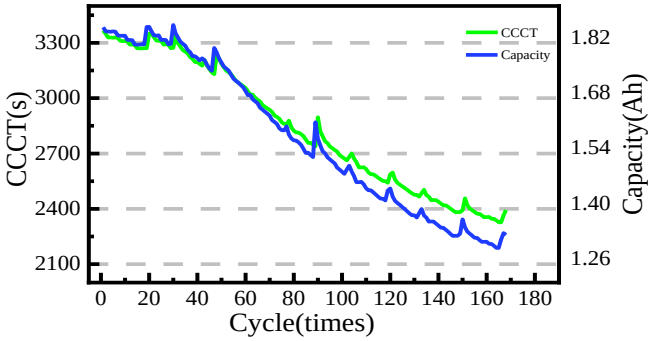

Figure 5. Trend plot of capacity and CCCT of B5 battery with the number of cycles

The decline trends of CCCT and battery capacity are more similar, and the maximum available capacity of the battery will affect the charging time in constant current charging mode. As the maximum available battery capacity decreases, the CCCT will become shorter, indicating an obvious positive correlation link between the both. Thus, CCCT can be used as a feature factor for estimating SOH. The CCCT of the battery is extracted from the current profile during constant-current charging as the first feature indicator and is denoted as $FI_{1(CCCT)}$, as shown in Equation (2).

$$\begin{cases} FI_{1(CCCT)} = \{\mathrm{CCCT}_1, \mathrm{CCCT}_2, \mathrm{CCCT}_3, \cdots \mathrm{CCCT}_i\} \\ \mathrm{CCCT}_i = t_{i,j} - t_{i,0} \end{cases} \tag{2}$$

In the above Equation (2), i denotes the total number of charging cycles. $t_{i,j}$ is the time corresponding to the end of the constant current charging process; $t_{i,0}$ is the time corresponding to the initial constant current charging.

FI_2: Constant voltage charging time (CVCT)

According to the charging voltage curve in Figure 4(a), it can be observed that the CVCT is gradually prolonged with the deepening of battery aging. From the comparison graph of battery capacity and CVCT trend with the number of cycles in Figure 6, it can be seen that the CVCT of a battery cycled 130 times has a significant prolongation trend than that of a battery cycled 40 times.

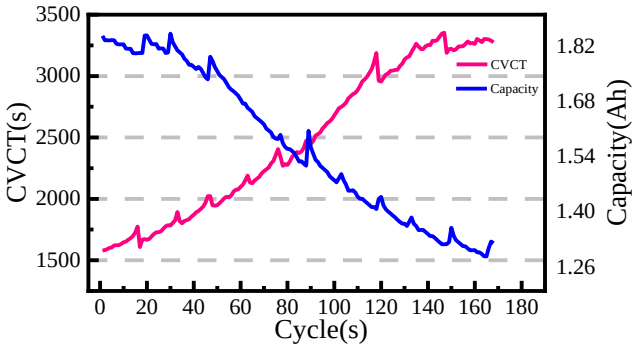

Figure 6. Trend plot of capacity and CVCT of B5 battery with the number of cycles

The CVCT and capacity decline show opposite trends. The maximum available capacity of the battery will affect the voltage situation in the constant voltage charging mode, with the decline of the maximum available capacity of the battery, the time taken to reach the specified voltage will rise, and there is an obvious negative correlation between the both. It indicates that CVCT can well express the trend of battery SOH decline. Thus, CVCT can be chosen as the characterization factor for SOH estimation, denoted as $FI_{2(CVCT)}$, as shown in Equation (3).

$$\begin{cases} FI_{2(CVCT)} = \{\mathrm{CVCT}_1, \mathrm{CVCT}_2, \mathrm{CVCT}_3, \cdots \mathrm{CVCT}_i\} \\ \mathrm{CVCT}_k = t_{k,j} - t_{i,0} \end{cases} \tag{3}$$

In the above Equation (3), k denotes the total number of charging cycles. $t_{k,j}$ is the time corresponding to the end of the CV charging process; $t_{i,0}$ is the time corresponding to the initial CV charging.

FI_3: Equal voltage drop time (EVDT)

From Figure 4(b), the discharge duration of the LIBs voltage drop from 3.5V to 2.8V is selected to plot the trend of B5 battery capacity and EVDT with the number of cycles, as shown in Figure 7. As can be seen in Figure 6, the greater the degree of aging of the battery, the shorter the time interval of equal voltage drop. The EVDT of LIBs with 160 cycles has a significant trend of decreasing compared to the EVDT with 40 cycles.

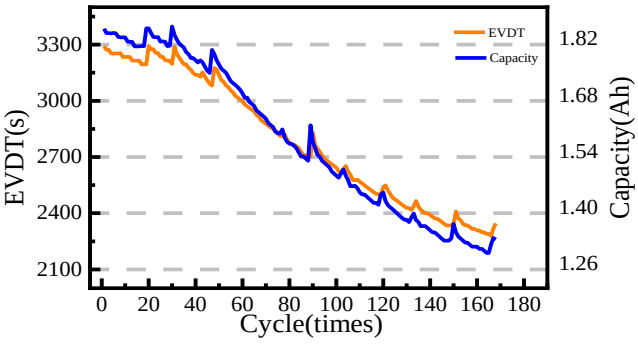

Figure 7. Trend plot of capacity and EVDT of B5 battery with the number of cycles

Both the EVDT and the battery capacity degradation curves show a decreasing trend with the charging and discharging cycles, and the similarity is very high. It shows that the maximum available capacity of the battery will affect the time taken for the equal voltage drop. As the maximum usable capacity of the battery decreases, the time taken for isovolts to drop will decrease, with a clear positive correlation between the two. It shows that EVDT can well characterize the SOH decline trend. Thus, EVDT can be chosen as the feature indicator for estimating SOH, denoted as $FI_{3(EVDT)}$. The mathematical expression of EVDT for the decline from 3.5V to 2.8V is shown in Equation (4).

$$\begin{cases} FI_{3(EVDT)} = \{\mathrm{EVDT}_1, \mathrm{EVDT}_2, \mathrm{EVDT}_3, \cdots \mathrm{EVDT}_i\} \\ \mathrm{EVDT}_i = t_{3.5} - t_{2.8} \end{cases} \tag{4}$$

In the Equation (4), $t_{3.5}$ is the time corresponding to the voltage of 3.5V during the discharge process; $t_{2.8}$ is the time corresponding to the voltage drop to 2.8V. The $FI3_{\mathrm{EVDT}}$ is the equal voltage drop discharge time series, where i denotes the number of cycles of the total discharge process.

2.3 Feature indicators correlation analysis

The analysis of the battery aging process and the comparative graphs of the feature indicators and the battery capacity decline trend show the degree of correlation between each feature factor and capacity. To further quantify the degree of correlation between the feature indicators and capacity, this paper uses the Pearson correlation coefficient to measure the degree of correlation between each feature factor and battery capacity. Its calculation formula is shown in Equation (5).

$$\mathrm{r} = \frac{\sum_{i=1}^{n}(x_i - \bar{x})\,(y_i - \bar{y})}{\sqrt{\sum_{i=1}^{n}(x_i - \bar{x})^2 (y_i - \bar{y})^2}} \tag{5}$$

In the Equation (5), n denotes is the number of variables; x_i and y_i are the mean values of variables x and y respectively, where the value of r ranges from -1 to 1. When $|r|$ is closer to 1, it indicates that the correlation between the both is higher.

According to Equation (5), the Pearson correlation coefficient values of CCCT, CVCT, and EVDT corresponding to each battery are calculated. Then, the degree of correlation between the features and FI with the battery capacity is evaluated based on the correlation coefficients, as shown in Table 2.

Table 2. Pearson correlation coefficients between each FI and battery capacity

Battery	$FI_{1(CCCT)}$	$FI_{2(CVCT)}$	$FI_{3(EVDT)}$

B5	0.9950	-0.9977	0.9872
B6	0.9901	-0.9998	0.9701
B7	0.9949	-0.9954	0.9990
B18	0.9727	-0.9981	0.9969

When the absolute value of the Pearson correlation coefficient reaches above 0.7, the two variables are considered to be strongly correlated. As can be seen from Table 2, the absolute values of correlation coefficients of FIs and battery capacity selected in this paper are above 0.7. $FI_{1(CCCT)}$ is positively and strongly correlated with battery capacity. $FI_{2(CVCT)}$ is negatively and strongly correlated with battery capacity. $FI_{3(EVDT)}$ is positively and strongly correlated with battery capacity. It shows that the FIs selected in this paper are strongly correlated with the battery capacity and can be used in the problem of estimating and predicting the battery SOH.

3. Theoretical Analysis

In this section, the SOH estimation of LIBs based on the SSA-CNN-Bi-LSTM model is constructed and the fundamentals and structures of the three main components: bi-directional long short-term memory networks, convolutional neural networks, and sparrow search algorithms are presented respectively.

3.1 Long Short-Term Memory Networks

LSTM is a kind of recurrent neural network with a special "gate" structure. A special "gate" structure can control the type and amount of feature information. The LSTM network achieves the function of filtering redundant information through the subtle use of "gate" logic control units, which to some extent overcomes the disadvantages of easy gradient disappearance and explosion. The LSTM consists of input gates, output gates, and forgetting gates. The structure of an LSTM unit is shown in Figure 8.

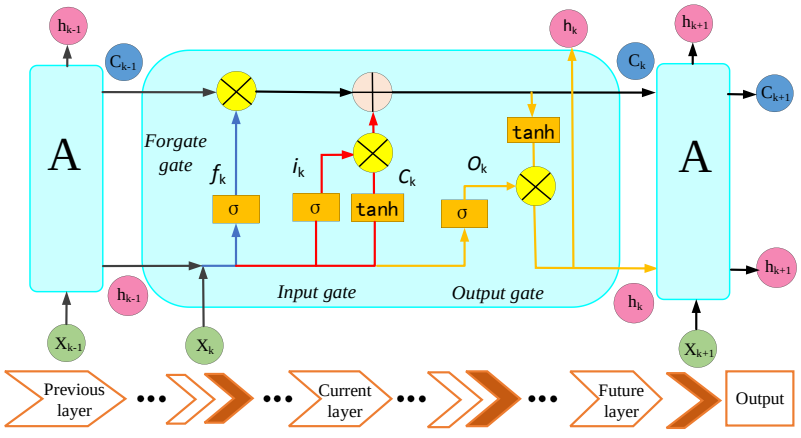

Figure 8. The internal structure of the LSTM

The first step of the LSTM network's iteration of information is to go through the forgetting gate f_k. The forgetting gate will judge and decide how much information from the state of C_{k-1} in the previous k-1 moments is retained to the information of C_k in the current k moments. By passing the input X_k of the current moment and the previous hidden layer state h_{k-1} to the activation function σ for processing, an element value between 0 and 1 is obtained for f_k. The specific information retention calculation formula is shown in Equation (6).

$$f_k = \sigma\left(W_f[h_{k-1}, X_k] + b_f\right) \tag{6}$$

When the value of f_k is 1, it means that the information is completely saved; when the value of f_k is 0, it means that the information is completely forgotten. In the next step, the output of the forgetting gate to the input gate i_k. The input gate will update the unit state. By passing the input X_k at the current moment and the hidden layer state h_{k-1} at the previous moment to the σ function and $tanh$ function, $\widetilde{C_k}$ and i_k are generated with the update of the cell state to get the update state C_k formula as shown in Equation (7).

$$\begin{cases} i_k = \sigma\left(W_i\left[h_{k-1}, X_k\right] + b_i\right) \\ \widetilde{C_k} = tanh\left(W_c\left[h_{k-1}, X_k\right] + b_c\right) \\ C_k = f_k \cdot C_{k-1} + \widetilde{C_k} \cdot i_k \end{cases} \tag{7}$$

Finally, the output gate O_k determines the information that can be output from the memory cell. By connecting the input X_k of the current moment and the previous hidden layer state h_{k-1} horizontally and passing it to the σ function, and then multiplying the outputs of the generated new unit state after passing it to the $tanh$ function to activate it, to decide the information that the hidden state h_k carries, and also to obtain the output formula of the current moment, as shown in Equation (8).

$$\begin{cases} O_k = \sigma\left(W_o\left[h_{k-1}, X_k\right] + b_o\right) \\ h_k = O_k \cdot tanh(C_k) \end{cases} \tag{8}$$

In the above Equations (6)-(8), W and b denote the weight matrix and the bias term of the forgetting gate, respectively.

3.2 Bi-directional Long Short-Term Memory Networks

Bi-LSTM is a variant structure of LSTM, and it can be very good to process the data of long time series from both positive and negative directions to infer more information. In Bi-

LSTM network contains the input layer, unidirectional LSTM with two opposite directions, a splicing layer, and the output layer as shown in Figure 9.

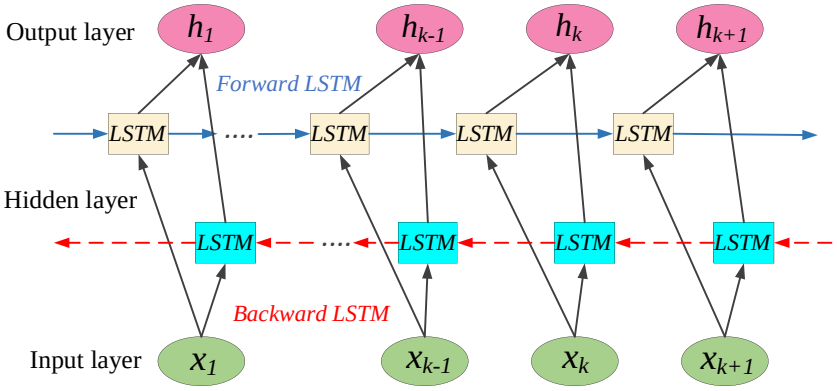

Figure 9. The internal structure of the Bi-LSTM

During network training, LSTM can only save and use the historical information of the aging process to predict the next moment output. However, Bi-LSTM can not only trace the historical information of the battery aging process but also consider future aging information. According to the principle of LSTM operation, Bi-LSTM first inputs the data forward to the forward LSTM layer and gets the output of the forward LSTM layer. Then, reverse the data into the reverse LSTM layer, get the reverse output, and then reverse the output again to get the output of the reverse LSTM layer. Finally, the output of the forward LSTM layer and the output of the reverse LSTM layer are linearly fused to get the final output. The specific formula is shown in Equation (9).

$$\begin{cases} \overrightarrow{h_k} = \overrightarrow{LSTM}\left(\overrightarrow{h_{k-1}}, \overrightarrow{X_k}\right) \\ \overleftarrow{h_k} = \overleftarrow{LSTM}\left(\overleftarrow{h_{k-1}}, \overleftarrow{X_k}\right) \\ h_k = W_k \cdot \overrightarrow{h_k} + V_k \cdot \overleftarrow{h_k} + b_k \end{cases} \tag{9}$$

In the Equation (9), $\overrightarrow{h_k}$ denotes the output result of the forward LSTM layer at moment k; $\overleftarrow{h_k}$ denotes the output result of the reverse LSTM layer at moment k; h_k denotes the output result of the state of the Bi-LSTM layer at moment k; W_k is the forward output weight; V_k is the reverse output weight; b_k is the bias terms of the output state of the Bi-LSTM layer.

3.3 Convolutional Neural Network

CNN is a special feed-forward deep neural network with powerful feature extraction capability to mine more abstract and advanced deep features from the input data. CNN is mainly composed of input and output layers and multiple hidden layers, where the hidden layers can

be divided into convolutional, pooling, and fully connected layers, and its structure is shown in Figure 10.

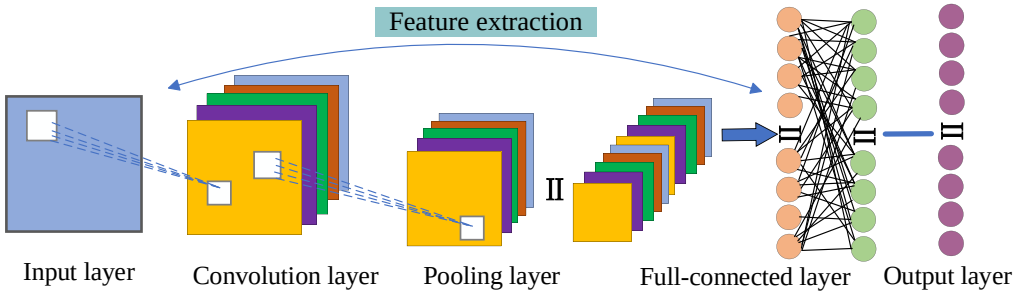

Figure 10. The architecture of the CNN estimation model

As a core layer of the CNN architecture, the convolutional layer contains multiple convolutional kernels within it. The convolutional layer extracts feature information from the input layer data (current, voltage, and temperature of the battery) by performing a linear, shift-invariant operation. Meanwhile, the convolutional kernel reduces the number of parameters and computations by locally weighting the input signal, which makes the CNN computation faster. The output h_i operation formula of the convolutional layer is shown in Equation (10).

$$h_i = f\left(\omega \times x_{i:i+g-1} + b\right) \tag{10}$$

In the Equation (10), f denotes the activation function; $x_{i:i+g-1}$ is denoted as the feature vector from i to $i+g-1$, in which g is the size of the convolution kernel; ω is the weight of the convolution kernel; and b is the bias parameter. The above operation yields the eigenvector matrix G.

The pooling layer performs a downsampling maximum pooling operation without compromising the recognition results, extracting the maximum value from each region to preserve the features. The pooling layer has feature invariance. By downsampling the feature data of the input convolutional layer, feature vectors of smaller dimensions are obtained by downsampling the input feature data without changing the features. So that the input feature data is downsampled without changing the characteristics, resulting in feature vectors with smaller dimensions.

The fully connected layer is the last step of the hidden layer located in the CNN. The features obtained through the above convolutional and pooling layers are integrated and then

the feature data is fed into the fully connected layer for classification and regression. Lastly, the prediction results are output through the output layer.

3.4 Sparrow Search Algorithm Optimization

SSA is an emerging intelligent optimization algorithm based on sparrow foraging and anti-enemy behaviors. The algorithm makes full use of the individual searching ability and mutual cooperation ability in the sparrow population and classifies the sparrow population into three types: discoverers, followers, and vigilantes. The flowchart of SSA for parameters (number of iterations, learning rate, number of hidden nodes in bidirectional LSTM layer, etc.) optimization of the CNN-Bi-LSTM hybrid neural model is shown in Figure 11.

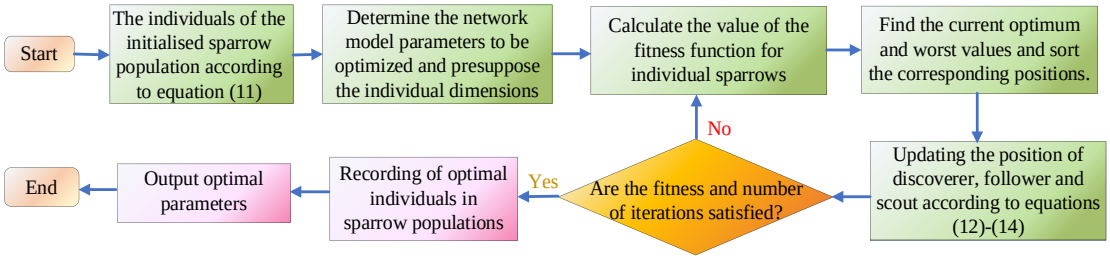

Figure 11. Flow chart of global parameter optimization of the SSA

Using SSA to simulate the process of sparrow flock foraging, a mathematical model is established in a D-dimensional space and the optimal solutions of some parameters are obtained within a certain range. Assuming a population consisting of n sparrows, the location X and the fitness value F_x of the sparrow population are expressed as shown in Equation (11).

$$\begin{cases} X = \begin{bmatrix} x_1^1 & x_1^2 & \cdots & x_1^D \\ x_2^1 & x_2^2 & \cdots & x_2^D \\ \cdots & \cdots & \cdots & \cdots \\ x_1^n & x_2^n & \cdots & x_n^D \end{bmatrix} \\ F_x = \begin{bmatrix} f([x_1^1 & x_1^2 & \cdots & x_1^D]) \\ f([x_2^1 & x_2^2 & \cdots & x_2^D]) \\ \cdots & \cdots & \cdots & \cdots \\ f([x_n^1 & x_2^n & \cdots & x_n^D]) \end{bmatrix} \end{cases} \tag{11}$$

In the Equation (11), D is denoted as the dimension of the parameter problem variable to be optimized; x_n^D is the position of the nth sparrow in the Dth dimension; and f denotes the fitness function of an individual sparrow, where $f([x_n^1 \quad x_2^n \quad \cdots \quad x_n^D])$ in the nth row denotes the degree value of the nth sparrow.

In the foraging process of sparrows, discoverers with higher fitness values are prioritized to obtain food and gain a larger foraging range. In each iteration, the sparrow as a finder gets the position updated as shown in Equation (12).

$$X_{i,z}^{t+1} = \begin{cases} X_{i,z}^{t} \cdot exp\left(\frac{i}{\alpha \cdot iter_{max}}\right), R_2 < ST \\ X_{i,z}^{t} + Q \cdot L, R_2 \geq ST \end{cases} \quad (12)$$

In the Equation (12), $R_2 \in [0,1]$ and $ST \in [0.5,1.0]$ represent the alarm value and alert threshold, respectively; when $R_2 < ST$ represents that when no natural enemy is posing a danger in the surrounding area, the discoverer can conduct an extended search; when $R_2 \geq ST$ represents that a discoverer in the population has discovered a natural enemy, and all the sparrows need to fly to the safe area quickly to take shelter. $X_{i,z}^{t}$ denotes the value of the z-th dimension of the ith sparrow at the t-th iteration; $exp\left(\frac{i}{\alpha \cdot iter_{max}}\right)$ denotes the exponential function with e as the base, where $iter_{max}$ is a constant, which denotes the maximal number of iterations. is a random number with a range of values from 0 to 1; L and Q represent the random numbers and matrices which obey the normal distribution, respectively.

The follower moves in the direction of the discoverer pursuing the physical object to obtain the corresponding food, and its position is updated as shown in Equation (13).

$$X_{i,z}^{t+1} = \begin{cases} X_{p}^{t+1} + \left|X_{i,z}^{t} - X_{p}^{t+1}\right| \cdot A^{T}(AA^{T})^{T} \cdot L, i \leq {}^{n}/_{2} \\ Q \cdot exp\left(\frac{X_{worst}^{t} - X_{i,z}^{t}}{\alpha \cdot iter_{max}}\right), i > {}^{n}/_{2} \end{cases} \quad (13)$$

In above Equation (13), X_p and X_{worst} represent the optimal foraging position of the finder and the worst position in the foraging environment, respectively; A is a unit matrix; when $i > {}^{n}/_{2}$, it indicates that the sparrow in the follower role has a low fitness value, has a poor position for obtaining food, and needs to change the foraging range; on the contrary, when $i \leq {}^{n}/_{2}$, it indicates that the sparrow in the follower role has a superior foraging position.

During the foraging process of a sparrow population, the vigilantes in the population will immediately perform vigilance behavior when they find predators around them. The position of the vigilant is also updated as the number of iterations changes, and the formula for a position update is shown in Equation (14).

$$X_{i,z}^{t+1} = \begin{cases} X_{best}^{t} + \gamma \cdot \left|X_{i,z}^{t} - X_{best}^{t}\right| \cdot A^{T}(AA^{T})^{T} \cdot L, f_i > f_g \\ X_{i,z}^{t} + K\left(\frac{\left|X_{i,z}^{t} - X_{worst}^{t}\right|}{(f_i - f_w) + \varepsilon}\right), f_i = f_g \end{cases} \quad (14)$$

In the Equation (14), f_g and f_w are the global optimal fitness value and the worst fitness value, respectively; X_{best} denotes the optimal position in the foraging environment, where γ is the step control parameter; K is the direction of controlling the sparrow's movement, with a range of -1 to 1; ε is the correction constant. When $f_i > f_g$, it indicates that the sparrow is at the edge of the population and is very vulnerable to predator attack; when $f_i = f_g$, it indicates that the sparrow discovers the predator at this time, realizes the danger of being preyed upon, and makes a vigilant behavior to approach other sparrows.

The optimal values of the model structural parameters after the SSA optimization search are shown in Table 3.

Table 3. Table of optimal parameters of the CNN-Bi-LSTM model after SSA optimization

Model structure	Parameter settings
CNN	Conv, Maxpooling, Relu
CNN convolution core size	3
Bi-LSTM layers	2
Batch size	28
Learning rate	0.01
Maximum number of iterations	1000
Activation function	Relu

3.5 Lithium-ion battery based on SSA optimized hybrid neural network model

Bi-LSTM can effectively extract historical useful information from the data in both directions, and CNN is more capable of deep feature extraction from the input data. Thus, a CNN-Bi-LSTM hybrid neural network model is proposed for SOH prediction of LIBs based on the fusion of prediction ideas and the advantages of the two kinds of models.

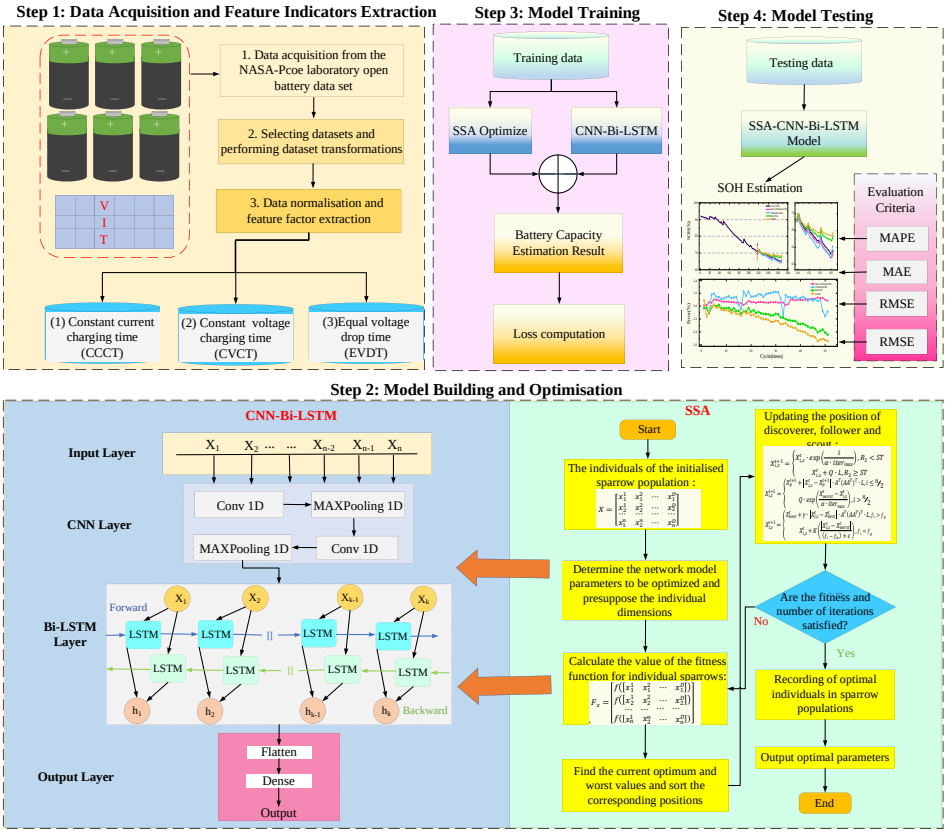

Figure 12. The flowchart of the proposed SOH estimation model

Since the parameters of the CNN-Bi-LSTM model are subjectively set by human beings, it is easy to fall into problems such as local optimal solutions, resulting in poor model accuracy. Different model parameters have a great impact on the battery SOH assessment results. To further improve the established SOH prediction model, SSA is used to optimize the model parameters and improve the model accuracy. The overall flow of the SSA-CNN-Bi-LSTM model for SOH prediction is shown in Figure 12.

Before SOH prediction, the NASA experimental dataset is first processed to extract the currents, voltages, temperatures, and calculated battery capacities from the charge/discharge cycles. Then, the data is feature extracted and analyzed into training and test sets. In the hyperparameter optimization step, the SSA algorithm is used to search for the optimal parameters of the CNN-Bi-LSTM model and then the model is trained. Thus the accurate SSA-CNN-Bi-LSTM model is formed and the SOH of the battery is estimated using the model. Finally, the proposed model is compared with other models used for SOH estimation.

4. Results and analysis of SOH prediction

To better validate the performance of the SSA-CNN-Bi-LSTM model for SOH estimation of LIBs, the error evaluation metrics such as maximum error (ME), mean absolute error (MAE), root mean square error (RMSE), and mean absolute percentage error (MAPE) are used to further compute and analyze the experimental results as shown in Equation (15).

$$\begin{cases} E_k = SOH_{real} - SOH_{predict} \\ ME = \max(|E_k|) \\ MAE = \dfrac{1}{n}\sum_{i=1}^{n}|E_k| \\ \mathrm{RMSE} = \sqrt{\dfrac{1}{n}\sum_{i=1}^{n}{E_k}^2} \\ MAPE = \dfrac{1}{n}\sum_{i=1}^{n}\left|\dfrac{E_k}{SOH_{real}}\right| \times 100\% \end{cases} \tag{15}$$

In Equation (15), SOH_{real} denotes the real value of SOH. $SOH_{predict}$ denotes the predicted value of SOH. n denotes the number of data to be predicted in the experiment. In particular, for the indicators RMSE, MAE, and MAPE, if their numerical values are closer to 0, it means that the prediction accuracy is more accurate.

To verify the effectiveness and superiority of the proposed SSA-CNN-Bi-LSTM model for SOH prediction of LIBs, other common neural network models will be added for comparison, including the LSTM model, Bi-LSTM model, and CNN-Bi-LSTM model. After adding feature metrics and battery capacity to the corresponding data for each of the above battery models, the former 70% of the data was used as the model training set and the latter 30% of the data was used as the model test set for SOH prediction. The prediction results of battery B5 are shown in Figure 13.

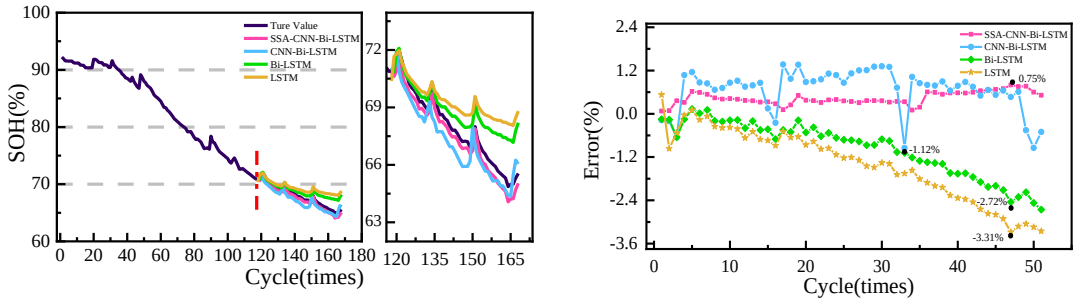

(a) (b)

Figure 13. The SOH estimation results with different methods for battery B5. (a) SOH prediction results; (b) SOH prediction error.

The SOH prediction process for the B5 battery is shown in Figure 13, taking the 116th cycle as the prediction starting point for estimating the SOH of the LIBs. From Figure 13, it

can be seen that although the LSTM model tends to estimate a certain true value when performing SOH prediction, the maximum estimation error reaches 3.31%, which cannot accurately pre-estimate the SOH operation of LIBs to the final stage. The maximum estimation error of the Bi-LSTM model is 2.72%. Compared to the LSTM model, the maximum estimation error is reduced by 0.59%. However, as the number of cycles increases, the Bi-LSTM model predictions deviate from the true value and have an obvious delay, which is less desirable. The maximum estimation error of the CNN-Bi-LSTM model is 1.12%. Compared with the Bi-LSTM model, the maximum estimation error of the CNN-Bi-LSTM model is reduced by 1.6%, and its prediction performance is significantly improved, but the prediction accuracy is still not high enough. The maximum estimation error of the SSA-CNN-Bi-LSTM model is 0.75%, and the prediction curve gradually fits the real value. Compared with the other three models, the prediction accuracy is significantly improved and the prediction accuracy is better.

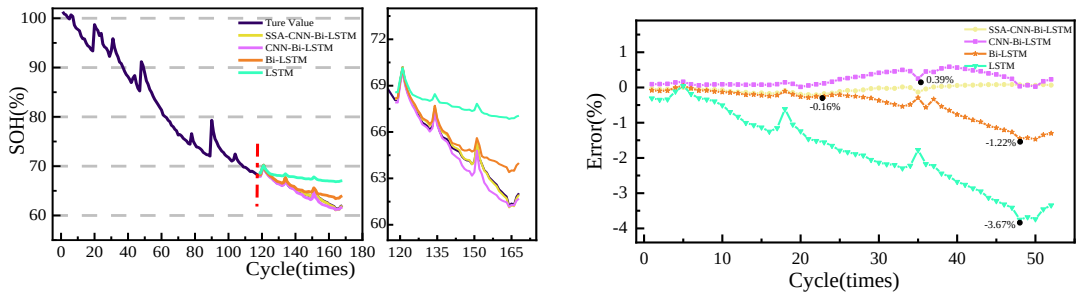

(a) (b)

Figure 14. The SOH estimation results with different methods for battery B6. (a) SOH prediction results; (b) SOH prediction error.

As can be visualized in Figure 14, the SSA-CNN-Bi-LSTM model is very close to the true value when predicting the battery SOH in the B6 battery, and the estimation is better than the other three comparative models. Taking the 117th cycle as the prediction starting point for estimating the SOH of LIBs, the estimation oscillations of the LSTM model and the Bi-LSTM model are large, and the maximum estimation errors reach 3.67% and 1.22%, respectively. The CNN-Bi-LSTM model is more stable in the middle and early stages of estimation and has a maximum estimation error of 0.39%. Compared with the Bi-LSTM model, the maximum estimation error of the CNN-Bi-LSTM model is reduced by 0.83%. However, as the number of cycles increases, the predicted values of the CNN-Bi-LSTM model gradually deviate from the true values, and the measurement accuracy is still not high enough. The maximum estimation

accuracy of the proposed SSA-CNN-BiLSTM model reaches 0.16% at this time, with significantly better fitting and smaller error fluctuations, which greatly improves the estimation accuracy of SOH for LIBs.

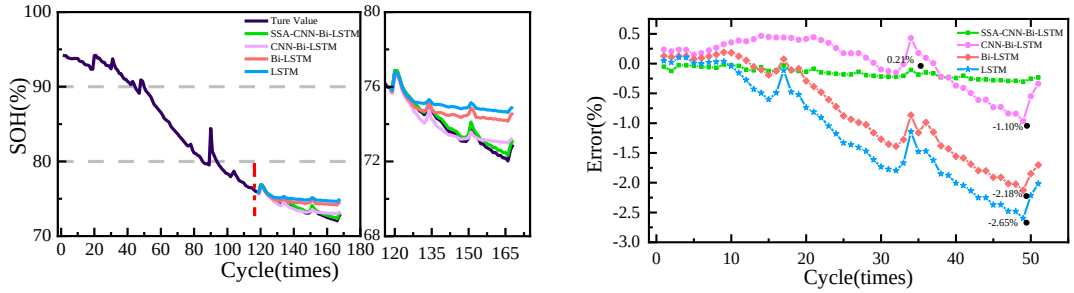

(a) (b)

Figure 15. The SOH estimation results with different methods for battery B7. (a) SOH prediction results; (b) SOH prediction error.

As shown in Figure 15, the SOH prediction process for the B7 battery uses the 115th cycle as the prediction starting point for predicting the SOH of the lithium-ion battery. The LSTM model and Bi-LSTM model predicted the starting point of the oscillation at the 115th cycle with a maximum error of 2.65% and 2.18%, respectively. The results of the CNN-Bi-LSTM model are less oscillating compared to the LSTM model and the Bi-LSTM model, with a maximum estimation error of 1.10%. Compared to the Bi-LSTM model, the maximum estimation error of the CNN-Bi-LSTM model is reduced by 0.35%. The SSA-CNN-Bi-LSTM model estimation error is estimated to be stable, oscillating within a certain region and closer to the true value curve, and its maximum estimation error is only 0.21%. As shown comprehensively, the SSA-CNN-Bi-LSTM model outperforms the LSTM model, the Bi-LSTM model, and the CNN-Bi-LSTM model in the case of the B7 battery, and it can more accurately estimate the SOH of the LIBs.

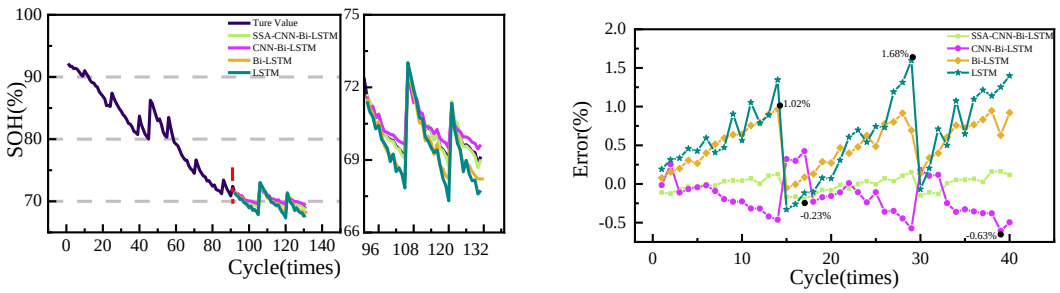

(a) (b)

Figure 16. The SOH estimation results with different methods for battery B18. (a) SOH prediction results; (b) SOH prediction error.

As shown in Figure 16, it can be intuitively obtained that the SOH prediction process of the B18 battery takes the 89th cycle as the starting point of prediction. The maximum error of the LSTM model reaches 1.68% and the estimation is unsatisfactory. The maximum error of the estimation of the Bi-LSTM model reaches 1.02%. Compared with the LSTM model, the Bi-LSTM model reduces the maximum estimation error by 0.66% and the estimation results are significantly improved, but there are violent oscillations in the range of the true value, which are unstable. Compared with the Bi-LSTM model, the results of the CNN-Bi-LSTM model do not have violent oscillation, the maximum estimation error decreases from 1.02% to 0.63%, and the maximum estimation error decreases by 0.39%. The prediction performance of the CNN-Bi-LSTM model is significantly improved, but the prediction accuracy is still not high enough. Compared with the CNN-Bi-LSTM model, the maximum estimation error of the SSA-CNN-Bi-LSTM model decreases from 0.63% to 0.23%, and the maximum estimation error decreases by 0.4%, and the error oscillations are very small, and the prediction curves are gradually fitted to the real values, and the model's estimation accuracy values are higher. It can be obtained that the SSA-CNN-Bi-LSTM model outperforms LSTM, Bi-LSTM, and CNN-Bi-LSTM models in estimating the SOH of LIBs under B18 batteries, and effectively improves the estimation accuracy of SOH of LIBs.

To visualize the SOH estimation error of each modeling method and illustrate the advantages of the SSA-CNN-Bi-LSTM model. Based on the experimental results, the estimation error of SOH estimation at each cycle is plotted using ME, MAPE, RMSE, and RMSE as the evaluation indexes, as shown in Figure 17.

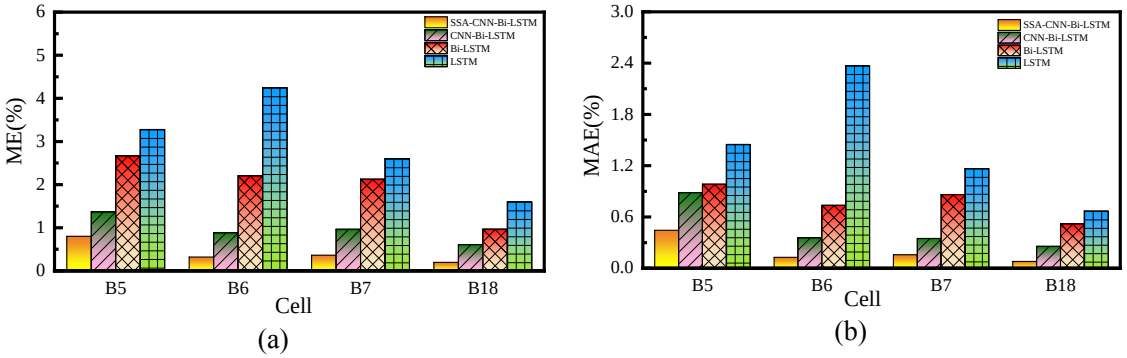

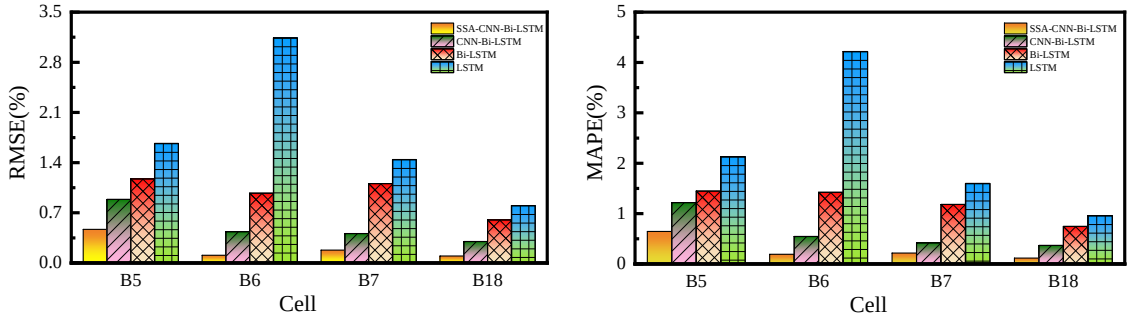

(c) (d)

Figure 17. Comparison of the results of the error in SOH prediction values for the four batteries. (a) ME; (b) MAE; (c) RMSE; (d)MAPE

The result plots in Figure 17 show the comparison results of the estimation performance evaluation metrics of the four models on the B5, B6, B07, and B18 battery number sets. As can be seen from the result plots, under the same conditions, the estimation performance of the SSA-CNN-Bi-LSTM model is significantly better than that of the CNN-Bi-LSTM model, the Bi-LSTM model, and the LSTM model, with better fitting and varying degrees of decreases in MAPE, MAE, and RMSE. Among these four cells, the maximum MAPE, MAE, and RMSE of the SSA-CNN-Bi-LSTM model are 0.6437%, 0.4431, and 0.4675%, respectively. Compared with the CNN-Bi-LSTM model, the MAPE, MAE, and RMSE of the SSA-CNN-Bi-LSTM model decreased by an average of 0.5733%, 0.4015%, and 0.4179%, respectively. Compared with the Bi-LSTM model, the MAPE, MAE, and RMSE of the SSA-CNN-Bi-LSTM model decreased by 0.8026%, 0.5394%, and 0.7041% on average, respectively. Compared with the LSTM model, the MAPE, MAE, and RMSE of the SSA-CNN-Bi-LSTM model decreased by 2.5736%, 2.293%, and 2.6715% on average, respectively. The fusion of the CNN model with the Bi-LSTM model optimizes and improves the accuracy of the algorithm, and the incorporation of SSA improves the prediction of the model. This advantage increases the possibility of applying the proposed method in practice.

5. Conclusions

To address the problem of accurate estimation of SOH for LIBs, this article proposes the prediction of SOH for lithium batteries based on the SSA to optimize the hybrid neural network model CNN-Bi-LSTM. In the SSA-CNN-Bi-LSTM model, CNN is used to extract the intrinsic features of the input data, Bi-LSTM is used to capture the relationship between the feature indicators and SOH in both directions, and SSA is used to optimize the structural parameters of

the hybrid model to achieve the accurate SOH estimation of LIBs. Experimental validation results with different models of battery datasets with different models show that the proposed SSA-CNN-Bi-LSTM model outperforms the LSTM model, the Bi-LSTM model, and the CNN-Bi-LSTM model, with the MAE lower than 0.5%, the MAPE lower than 0.7%, and the RMSE lower than 0.5%, and it can predict the SOH of LIBs more accurately.

Future research will further consider uncertainties such as battery aging degree, charge/discharge multiplier, and environmental temperature, and combine them with the mechanism model to establish a more accurate SOH estimation model for LIBs.

Acknowledgments

This work is supported by the National Natural Science Foundation of China (No. 62173281), Sichuan Provincial Science and Technology Program (No. 24NSFSC0024, 23ZDYF0734, 23NSFSC1436), Dazhou City School Partnership Program (No. DZXQHZ006), Technology Pole Talent Summit Program (No. KJCRCFH08), and Robert Gordon University.

Reference:

1. Wei, H., et al., Design and validation of a battery management system for solar-assisted electric vehicles. Journal of Power Sources, 2021. **513**.
2. Xie, K., et al., A method for measuring and evaluating the fault response performance of battery management system. Energy Reports, 2022. **8**: p. 639-649.
3. Zhou, L., et al., State Estimation Models of Lithium-Ion Batteries for Battery Management System: Status, Challenges, and Future Trends. Batteries, 2023. **9**(2).
4. Zou, Y., et al., Advancements in Artificial Neural Networks for health management of energy storage lithium-ion batteries: A comprehensive review. Journal of Energy Storage, 2023. **73**.
5. Wang, Y., et al., System identification and state estimation of a reduced-order electrochemical model for lithium-ion batteries. eTransportation, 2023. **18**.
6. Wang, Y., et al., Perspectives and challenges for future lithium-ion battery control and management. eTransportation, 2023. **18**.
7. Lin, Z., D. Li, and Y. Zou, Energy efficiency of lithium-ion batteries: Influential factors and long-term degradation. Journal of Energy Storage, 2023. **74**.
8. Sharma, P. and B.J. Bora, A Review of Modern Machine Learning Techniques in the Prediction of Remaining Useful Life of Lithium-Ion Batteries. Batteries, 2022. **9**(1).
9. Ramasubramanian, A., et al., Lithium Diffusion Mechanism through Solid–Electrolyte Interphase in Rechargeable Lithium Batteries. The Journal of Physical Chemistry C, 2019. **123**(16): p. 10237-10245.
10. Liu, Y., et al., State-of-health estimation of lithium-ion batteries based on electrochemical impedance spectroscopy: a review. Protection and Control of Modern

Power Systems, 2023. **8**(1).
11. Bao, X., et al., Hybrid deep neural network with dimension attention for state-of-health estimation of Lithium-ion Batteries. Energy, 2023. **278**.
12. Fan, M., et al., State of Health Estimation of Lithium-Ion Battery Based on Electrochemical Impedance Spectroscopy. Energies, 2023. **16**(8).
13. Guo, F., et al., State of Health estimation method for lithium batteries based on electrochemical impedance spectroscopy and pseudo-image feature extraction. Measurement, 2023. **220**.
14. Yi, Z., et al., Sensing as the key to the safety and sustainability of new energy storage devices. Protection and Control of Modern Power Systems, 2023. **8**(1).
15. Chen, D., et al., Remaining useful life prediction of the lithium-ion battery based on CNN-LSTM fusion model and grey relational analysis. Electronic Research Archive, 2023. **31**(2): p. 633-655.
16. Hu, L., W. Wang, and G. Ding, RUL prediction for lithium-ion batteries based on variational mode decomposition and hybrid network model. Signal, Image and Video Processing, 2023. **17**(6): p. 3109-3117.
17. Zhao, S., et al., Lithium-Ion Battery State-of-Health Estimation Method Using Isobaric Energy Analysis and PSO-LSTM. Journal of Electrical and Computer Engineering, 2023. **2023**: p. 1-11.
18. Nuroldayeva, G., et al., State of Health Estimation Methods for Lithium-Ion Batteries. International Journal of Energy Research, 2023. **2023**: p. 1-21.
19. Liu, K., L. Kang, and D. Xie, Online State of Health Estimation of Lithium-Ion Batteries Based on Charging Process and Long Short-Term Memory Recurrent Neural Network. Batteries, 2023. **9**(2).
20. Ma, G., et al., A Transfer Learning-Based Method for Personalized State of Health Estimation of Lithium-Ion Batteries. IEEE Transactions on Neural Networks and Learning Systems, 2022: p. 1-11.
21. Su, S., et al., A Hybrid Battery Equivalent Circuit Model, Deep Learning, and Transfer Learning for Battery State Monitoring. IEEE Transactions on Transportation Electrification, 2023. **9**(1): p. 1113-1127.
22. Bao, Z., et al., A New Hybrid Neural Network Method for State-of-Health Estimation of Lithium-Ion Battery. Energies, 2022. **15**(12).
23. Bi, J., J.-C. Lee, and H. Liu, Performance Comparison of Long Short-Term Memory and a Temporal Convolutional Network for State of Health Estimation of a Lithium-Ion Battery using Its Charging Characteristics. Energies, 2022. **15**(7).
24. Sun, X., et al., Summary of Health-State Estimation of Lithium-Ion Batteries Based on Electrochemical Impedance Spectroscopy. Energies, 2023. **16**(15).
25. Yao, F., et al., Online health estimation strategy with transfer learning for operating lithium-ion batteries. Journal of Power Electronics, 2023. **23**(6): p. 993-1003.
26. Zhang, C.-y., et al., Improved Particle Swarm Optimization-Extreme Learning Machine Modeling Strategies for the Accurate Lithium-ion Battery State of Health Estimation and High-adaptability Remaining Useful Life Prediction. Journal of The Electrochemical Society, 2022. **169**(8).
27. Xu, Z., et al., Co-estimating the state of charge and health of lithium batteries through

combining a minimalist electrochemical model and an equivalent circuit model. Energy, 2022. **240**.
28. Yu, X., T. Ai, and K. Wang, Application of nanogenerators in acoustics based on artificial intelligence and machine learning. APL Materials, 2024. **12**(2).
29. Prasad, G.K. and C.D. Rahn, Model based identification of aging parameters in lithium ion batteries. Journal of Power Sources, 2013. **232**: p. 79-85.
30. Tran, M.-K., et al., A comprehensive equivalent circuit model for lithium-ion batteries, incorporating the effects of state of health, state of charge, and temperature on model parameters. Journal of Energy Storage, 2021. **43**.
31. Virkar, A.V., A model for degradation of electrochemical devices based on linear non-equilibrium thermodynamics and its application to lithium ion batteries. Journal of Power Sources, 2011. **196**(14): p. 5970-5984.
32. Ashwin, T.R., Y.M. Chung, and J. Wang, Capacity fade modelling of lithium-ion battery under cyclic loading conditions. Journal of Power Sources, 2016. **328**: p. 586-598.
33. Chu, A., et al., Stochastic capacity loss and remaining useful life models for lithium-ion batteries in plug-in hybrid electric vehicles. Journal of Power Sources, 2020. **478**.
34. Hu, C., et al., State of Charge Estimation for Lithium-Ion Batteries Based on TCN-LSTM Neural Networks. Journal of The Electrochemical Society, 2022. **169**(3).
35. Kim, S., et al., Improved State-of-health prediction based on auto-regressive integrated moving average with exogenous variables model in overcoming battery degradation-dependent internal parameter variation. Journal of Energy Storage, 2022. **46**.
36. Li, Q., et al., State of health estimation of lithium-ion battery based on improved ant lion optimization and support vector regression. Journal of Energy Storage, 2022. **50**.
37. Piao, C., et al., Analysis of Real-Time Estimation Method Based on Hidden Markov Models for Battery System States of Health. Journal of Power Electronics, 2016. **16**(1): p. 217-226.
38. Qin, W., et al., Remaining useful life prediction for lithium-ion batteries using particle filter and artificial neural network. Industrial Management & Data Systems, 2019. **120**(2): p. 312-328.
39. Yang, D., et al., A novel Gaussian process regression model for state-of-health estimation of lithium-ion battery using charging curve. Journal of Power Sources, 2018. **384**: p. 387-395.
40. Long, B., et al., An improved autoregressive model by particle swarm optimization for prognostics of lithium-ion batteries. Microelectronics Reliability, 2013. **53**(6): p. 821-831.
41. Qin, S., State of Charge estimation of lithium-ion power battery based on online parameter identification method and BP neural network. International Journal of Electrochemical Science, 2022.
42. Li, X., et al., Online Prediction of Electric Vehicle Battery Failure Using LSTM Network. Energies, 2023. **16**(12).
43. Nguyen Van, C. and D.T. Quang, Estimation of SoH and internal resistances of Lithium ion battery based on LSTM network. International Journal of Electrochemical Science, 2023. **18**(6).

44. Ma, N., H. Yin, and K. Wang, Prediction of the Remaining Useful Life of Supercapacitors at Different Temperatures Based on Improved Long Short-Term Memory. Energies, 2023. **16**(14).
45. Zhang, L., et al., Accurate Prediction Approach of SOH for Lithium-Ion Batteries Based on LSTM Method. Batteries, 2023. **9**(3).
46. Tang, R., et al., Prediction of Battery SOH and RUL Based on Cooperative Characteristics in Voltage-Temperature-Time Dimensions. Journal of The Electrochemical Society, 2023. **170**(6).
47. Zhang, Y., et al., Weight optimized unscented Kalman filter for degradation trend prediction of lithium-ion battery with error compensation strategy. Energy, 2022. **251**.
48. Guo, Y., et al., Online estimation of SOH for lithium-ion battery based on SSA-Elman neural network. Protection and Control of Modern Power Systems, 2022. **7**(1).
49. Guo, Y., et al., State of health estimation for lithium-ion battery based on Bi-directional long short-term memory neural network and attention mechanism. Energy Reports, 2022. **8**: p. 208-215.
50. Guo, Y., et al., A state□of□health estimation method considering capacity recovery of lithium batteries. International Journal of Energy Research, 2022. **46**(15): p. 23730-23745.
51. Mei, P., et al., A Learning-Based Vehicle-Cloud Collaboration Approach for Joint Estimation of State-of-Energy and State-of-Health. Sensors (Basel), 2022. **22**(23).
52. Park, M.-S., J.-k. Lee, and B.-W. Kim, SOH Estimation of Li-Ion Battery Using Discrete Wavelet Transform and Long Short-Term Memory Neural Network. Applied Sciences, 2022. **12**(8).
53. Zhang, C., et al., Fault Diagnosis of Nuclear Power Plant Based on Sparrow Search Algorithm Optimized CNN-LSTM Neural Network. Energies, 2023. **16**(6).
54. Sun, S., et al., Prediction of Battery SOH by CNN-BiLSTM Network Fused with Attention Mechanism. Energies, 2022. **15**(12).
55. Hou, J., et al., Parameter Identification of Lithium Battery Model Based on Chaotic Quantum Sparrow Search Algorithm. Applied Sciences, 2022. **12**(14).
56. Jia, J., et al., Improved sparrow search algorithm optimization deep extreme learning machine for lithium-ion battery state-of-health prediction. iScience, 2022. **25**(4).
57. Li, Y., et al., Research on state-of-charge Estimation of Lithium-ion Batteries Based on Improved Sparrow Search Algorithm-BP Neural Network. International Journal of Electrochemical Science, 2022. **17**(8).
58. Liu, Y., et al., A novel remaining useful life prediction method for lithium-ion battery based on long short-term memory network optimized by improved sparrow search algorithm. Journal of Energy Storage, 2023. **61**.
59. Zhang, H., et al., State of health estimation of lithium-ion batteries based on modified flower pollination algorithm-temporal convolutional network. Energy, 2023. **283**.
60. Yue, Y., et al., Review and empirical analysis of sparrow search algorithm. Artificial Intelligence Review, 2023. **56**(10): p. 10867-10919.